OPEN ACCESS



On the Short-scale Spatial Variability of Electron Inflows in Electron-only Magnetic Reconnection in the Turbulent Magnetosheath Observed by MMS

P. S. Pyakurel¹, T. D. Phan¹, J. F. Drake², M. A. Shay³, M. Øieroset¹, C. C. Haggerty⁴, J. Stawarz⁵, J. L. Burch⁶, R. E. Ergun⁷, D. J. Gershman⁸, B. L. Giles⁷, R. B. Torbert⁹, R. J. Strangeway¹⁰, and C. T. Russell⁹, and C. T. Russell⁹, and C. T. Russell⁹, Space Sciences Laboratory, University of California, Berkeley, CA, 94720, USA; pspyakurel@berkeley.edu

Department of Physics and the Institute for Physical Science and Technology, University of Maryland, College Park, MD, 20742, USA

Department of Physics and Astronomy and the Bartol Research Center, University of Delaware, Newark, DE, 19716, USA

Institute for Astronomy, University of Hawai'i, Manoa, Honolulu, HI, 96822, USA

Southwest Research Institute, San Antonio, TX, 78238, USA

Vuniversity of Colorado LASP, Boulder, CO, 80303, USA

NASA Goddard Space Flight Center, Greenbelt, MD, 20771, USA

University of New Hampshire, Durham, NH, 03824, USA

Openation of Earth, Planetary, and Space Sciences, University of California, Los Angeles, CA, USA

Received 2022 September 16; revised 2023 January 19; accepted 2023 January 23; published 2023 April 28

Abstract

We investigate the detailed properties of electron inflow in an electron-only reconnection event observed by the four Magnetospheric Multiscale (MMS) spacecraft in the Earth's turbulent magnetosheath downstream of the quasi-parallel bow shock. The lack of ion coupling was attributed to the small-scale sizes of the current sheets, and the observed bidirectional super-Alfvénic electron jets indicate that the MMS spacecraft crossed the reconnecting current sheet on both sides of an active X-line. Remarkably, the MMS spacecraft observed the presence of large asymmetries in the two electron inflows, with the inflows (normal to the current sheet) on the two sides of the reconnecting current layer differing by as much as a factor of four. Furthermore, even though the four MMS spacecraft were separated by less than seven electron skin depths, the degree of inflow asymmetry was significantly different at the different spacecraft. The asymmetry in the inflow speeds was larger with increasing distances downstream from the reconnection site, and the asymmetry was opposite on the two sides of the X-line. We compare the MMS observations with a 2D kinetic particle-in-cell (PIC) simulation and find that the asymmetry in the inflow speeds stems from in-plane currents generated via the combination of reconnection-mediated inflows and parallel flows along the magnetic separatrices in the presence of a large guide field.

Unified Astronomy Thesaurus concepts: Solar-terrestrial interactions (1473)

1. Introduction

Magnetic reconnection is an explosive energy conversion process that energizes particles via the release of magnetic energy. In the standard model of reconnection, magnetic field lines diffuse and reconnect at two disparate scales, namely the ion inertial length (d_i) scales and the electron inertial length (d_e) scales that approximately span the ion diffusion region (IDR) and the electron diffusion region (EDR; Vasyliunas 1975; Sonnerup 1979; Shay et al. 1998), respectively.

In contrast to the standard model of reconnection, recent observations of thin current sheets in Earth's highly turbulent magnetosheath region downstream of quasi-parallel bow shocks (Phan et al. 2018) revealed diverging electron outflow jets from a reconnection X-line, at speeds comparable to the electron Alfvén speed, but without the associated ion jets. The electron-scale reconnection current sheet was not embedded in an ion-scale current sheet as expected for a crossing of the EDR associated with standard ion-coupled reconnection (Burch et al. 2016; Eriksson et al. 2016; Wilder et al. 2017), and was therefore dubbed "electron-only reconnection." However, observations at Earth's bow shock of electron-only reconnection with no ion response inside ion-scale current sheets

Original content from this work may be used under the terms of the Creative Commons Attribution 4.0 licence. Any further distribution of this work must maintain attribution to the author(s) and the title of the work, journal citation and DOI.

(Gingell et al. 2019; Wang et al. 2019) indicate that having wider current sheet at scales comparable to the ion inertial scale is not sufficient to induce ion coupling.

2D reconnection simulations have indicated that the length of the current sheet (in the outflow direction) plays an important role in whether ions become decoupled from the reconnecting magnetic field, revealing that ions remain decoupled from the magnetic field when the length of the current sheet (in the outflow direction) is only a few inertial lengths (d_i ; Mandt et al. 1994) up to around ten ion inertial lengths (Pyakurel et al. 2019), depending on the plasma conditions. In the bow shock and turbulent magnetosheath (He et al. 2011; Stawarz et al. 2019), correlation length scales of the order $1-10 \ d_i$ were measured, indicating that magnetosheath turbulence is statistically a favorable environment to produce electron-only reconnection (Stawarz et al. 2022).

One important factor regarding the role of electron-only reconnection in the dissipation of turbulent fluctuations is the reconnection rate. 2D particle-in-cell (PIC) simulations of electron-only reconnection have shown that the reconnection rate can be significantly higher for electron-only reconnection in comparison with ion-coupled reconnection, with inflow rates increasing to values greater than 0.6 of the ion Alfvén speed, depending on the length of the current sheet (Pyakurel et al. 2019). A recent observational study of electron inflows using Magnetospheric Multiscale (MMS) spacecraft data (Burch et al. 2020) have

also used electron inflows (normal to the current sheet) to infer the reconnection rate.

In the present study, we examine the characteristics of electron inflows and how they vary around the X-line in an electron-only reconnection event that occurred on 2016 December 26 observed by MMS, previously reported by Phan et al. (2018). We investigate new observational features of the event and use PIC simulations to understand the reconnection geometry and particle signatures generated in electron-only reconnection. The four MMS spacecraft observations reveal significant asymmetries in the inflows from the two sides of the current sheet. Using MMS observations and PIC simulation findings, we investigate how such asymmetries in the inflow velocities are generated in electron-only reconnection with a large (≥1) guide field.

2. Data and Methods

2.1. Instrumentation

The study uses burst-mode magnetic field data from the MMS fluxgate magnetometer at 128 samples s⁻¹ (Russell et al. 2016), plasma data from the Fast Plasma Investigation (FPI) instruments at 37.5 ms resolution for ions and 7.5 ms for electrons (Rager et al. 2018), and data from the electric field instrument at 8192 samples s⁻¹ (Torbert et al. 2016). The MMS ion and electron measurements are highly accurate and the current density can be reliably obtained from the differential ion and electron velocities (e.g., Lavraud et al. 2016; Phan et al. 2016).

2.2. Coordinate System of Observations

The event occurred in the magnetosheath region downstream of the quasi-parallel bow shock on 2016 December 9 at around 09:03:54 UT. The reconnection current sheet observations are presented in the current-sheet (LMN) coordinate system, where the current sheet normal is along N, L is along the antiparallel magnetic field direction and $M = N \times L$ is in the out-of-plane ("X-line") direction. A common LMN coordinate system is used to compare observations from the four spacecraft, determined from the MMS3 crossing of the current sheet at 09:03:54.270–09:03:54.365 UT, with L = (-0.091, 0.87, $(0.49)_{GSE}$, $M = (-0.25, -0.49, 0.83)_{GSE}$, and N = (0.96, -0.05, -0.05)0.27)_{GSE}. The LMN coordinate system was determined using a hybrid minimum-variance method, which often works best in low-magnetic-shear current sheets (Gosling & Phan 2013). In this method, the normal, N, direction was determined from $B_1 \times B_2/|B_1 \times B_2|$, where B_1 and B_2 were the magnetic field vectors immediately adjacent to the exhaust boundaries. The direction of the X-line (denoted by the M-direction) is found from the cross product of unit vectors in the N and L'directions, where L' is the maximum variance direction determined from the minimum-variance analysis. Finally, the exhaust outflow (L) direction is obtained from the cross product of the unit vectors in the M- and N-directions.

The use of a common LMN coordinate system is justified based on the fact that the components of the LMN coordinates at individual spacecraft differ from each other by less than 4°. Furthermore, the main findings in terms of the inflow velocities are qualitatively the same, regardless of the LMN coordinate system determined from any spacecraft. The MMS3 LMN is used because the MMS3 current sheet crossing time is between those of the other spacecraft.

2.3. PIC Simulations

We performed simulations in 2D using the PIC code P3D (Zeiler et al. 2002). We normalized the magnetic field and density to $B_0 = 1$ and $n_0 = 1$, respectively, time to $\Omega_{\rm ce}^{-1}={\rm m_e}c/(eB_0)$, speed to $c_{\rm Ae}=\sqrt{B_0^2/4\pi m_{\rm e}n_0}$ (exceptions: see the caption of Figures 3(i)–(1)), length to $d_{\rm e}=c_{\rm Ae}/\Omega_{\rm ce}$, electric field to $E_0 = c_{Ae}B_0/c$, where c is the speed of light, and temperature to $T_0 = m_{\rm e}$ $c_{\rm Ae}^2$. A realistic mass ratio $m_{\rm i}/m_{\rm e} = 1836$, 10^3 particles per grid (ppg), speed of light $c/c_{Ae} = 2.33$, and uniform density n = 1 are chosen. The ion and electron temperatures are $T_i = 2.7$ and $T_e = 0.27$, respectively, giving the Debye length $\lambda_{\rm De} = \sqrt{2T_{\rm e}/c} \simeq 0.31$ and the electron gyro-radius $\rho_{\rm e}=\sqrt{2T_{\rm e}}\simeq 0.73$. The domain lengths $L_{\rm x}\times L_{\rm y}$ are 42.84 $d_{\rm e}\times$ 42.84 $d_{\rm e}$, with grid scale $\Delta\simeq 0.1674$, and time step $dt \simeq 0.06$. We use periodic boundary conditions in all directions and force-free initial conditions, with the initial reconnecting magnetic field given by $B_L = \tanh[(y - y)]$ $0.25 L_y / w_0 - \tanh[(y - 0.75 L_y) / w_0] - 1$ and the guide (outof-plane) magnetic field given by $B_{\rm M} = \sqrt{1 + B_{\rm g}^2 - B_{\rm L}^2}$, where $w_0 \simeq 1 d_e$ is the half-width of the initial current sheet and $B_{\rm g} = 1$ is the asymptotic guide field (see the discussion in Section 3.5 for our selection of guide field, which is smaller than the MMS observations of $B_g = 8$). The simulation results are shown in the spacecraft coordinate system where M points into the page.

The initial current sheet consists solely of electron currents with ions as a neutralizing background where magnetic reconnection onset is from particle noise.

3. Results: Observations and Simulation

3.1. Large-scale Context

On 2016 December 9, the MMS spacecraft sampled turbulent current sheets in Earth's subsolar magnetosheath region downstream of a quasi-parallel shock. Within a 21 minute interval alone (see Figure 2 in Phan et al. 2018), hundreds of intense electron-scale current sheets were detected and some of them showed evidence of electron-only reconnection without ion coupling. One event at around 09:03:54 UT showed convincing evidence for electron-only reconnection with the detection of bidirectional electron jets. Such fortuitus events are generally difficult to detect because the probes must traverse on the opposite sides of the X-line when the interspacecraft separations are only $\sim 7\,\mathrm{km}$ ($\sim 7\,\mathrm{d_e}$).

The reconnecting current sheet (and the X-line) was embedded in the magnetosheath flows. Therefore, a dynamic spacecraft configuration must be determined to examine the detailed properties of the inflow velocities at various distances from the X-line. In the following sections, we present new multi-spacecraft observations to show that the thin current sheet at around 09:03:54 UT exhibited strong electron inflow variability within a distance of a few $d_{\rm e}$. We will compare the observations with corresponding simulation findings to understand the inflow velocity properties.

3.2. Spacecraft Separation and Distance from the X-line

The relative spacecraft separation based on the current sheet coordinate system (LMN) determined from MMS3 are shown in Figure 1(n). In this event, the electron inertial length $d_{\rm e}$ is approximately 1 km with an upstream density of $\sim\!20\,{\rm cm}^{-3}$. The relative distances between MMS1, MMS4, MMS2, and

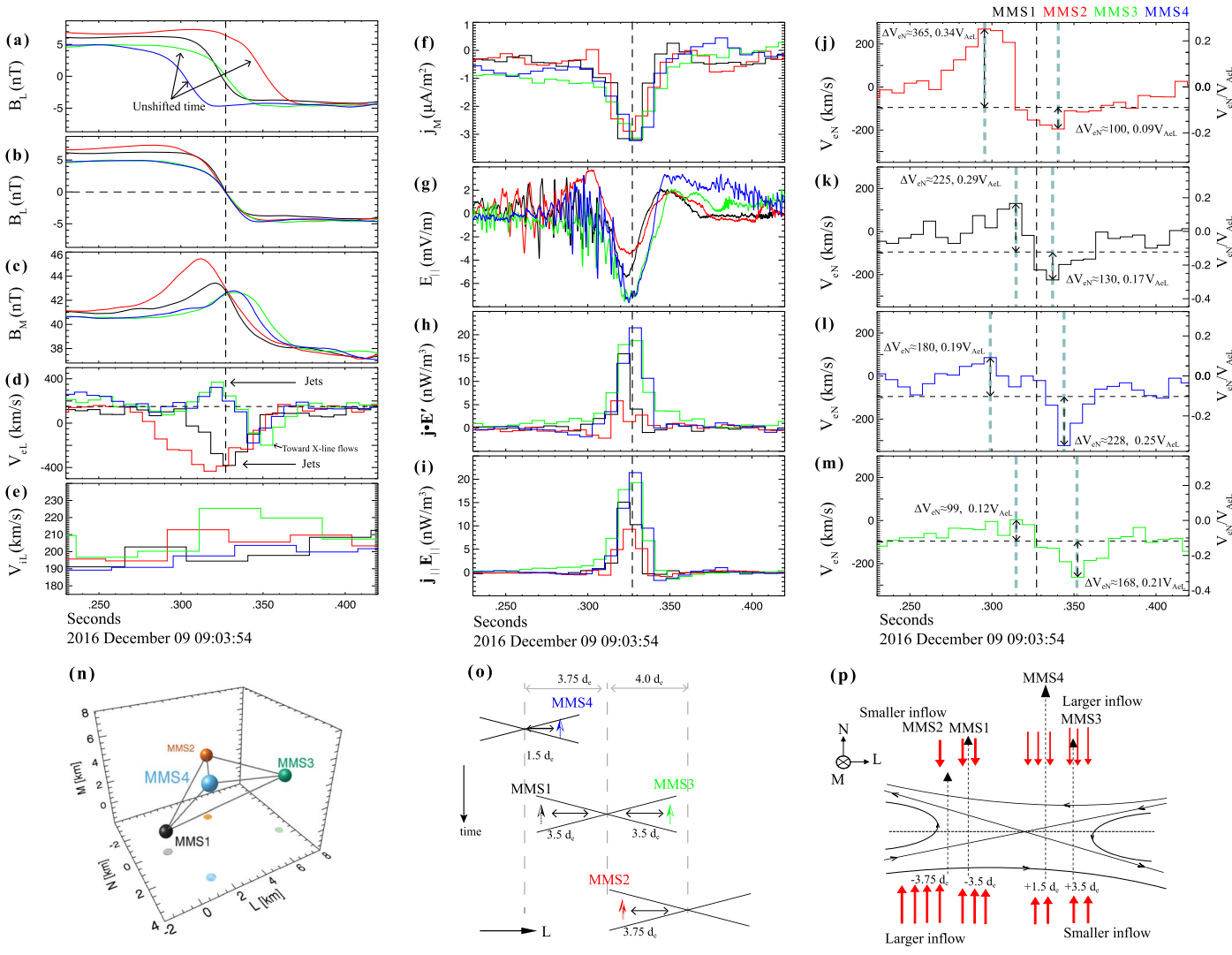


Figure 1. Multi-spacecraft observations of the reconnecting current sheet in the LMN coordinate system in the unshifted (a) and shifted (b-m) time frames based on the LMN coordinate system obtained from MMS3 measurements. (a), (b) The reconnecting magnetic fields B_L , (c) guide field B_M , (d) the electron outflow V_{eL} with an ambient electron flow of about +150 km s⁻¹ (dashed horizontal; see more discussion in Section 3.3), (e) ion flows, (f) the out-of-plane current j_M , (g) enhanced parallel electric field E_{\parallel} , (h) enhanced magnetic-to-particle energy conversion $j \cdot E' \equiv j \cdot (E + V_e \times B)$, and (i) $j_{\parallel} E_{\parallel}$ are shown for all four spacecraft. Bipolar inflowing electrons V_{eN} (j-m) with the background convection speed of -95 km s⁻¹ (dashed horizontal lines) are observed for all spacecraft. The inflows for all spacecraft are also shown in the normalized units of electron Alfvén speed given by $V_{AeL} = [B_{L1}B_{L2}(B_{L1} + B_{L2})/(\mu_o\rho_1B_{L2} + \mu_o\rho_2B_{L1})]^{1/2}$, with subscripts 1 and 2 denoting the locations of the first and second pink dashed lines, respectively. (n) Spacecraft separation determined from the LMN coordinate system. (o) Dynamic spacecraft orientation showing their distances from the X-line as each probe crosses the reconnection current sheet. The dashed vertical lines are the locations of the X-line traversing with the background flow speed of +150 km s⁻¹. (p) Schematic of the spacecraft orientations along the L-direction in a stationary X-line frame. The red arrows represent the inflowing electron velocities, showing larger asymmetries away from the X-line and symmetric inflowing electron velocities closer to the X-line.

MMS3 are 1.3 d_e , 2.5 d_e , and 3.2 d_e , respectively, in the *L*-direction. However, Figure 1(n) does not reveal the location of the spacecraft relative to the X-line.

If one assumes that the X-line is stationary in the frame of the bulk electron flow, then the X-line would drift in the outflow (L) direction with the background electron velocity along L measured outside the current sheet. Thus, the locations of the spacecraft relative to the X-line can be estimated by considering the bulk motion of the X-line, and the relative times the four spacecraft crossed the current sheet.

The first probe to sample the reconnection current sheet was MMS4 as seen in Figure 1(a). MMS1 and MMS3 crossed the current sheet at nearly the same time, 250 ms after MMS4. We estimate that the X-line moved \sim 3.75 $d_{\rm e}$ in the +L-direction during this time since the observed background drift speed was \sim +150 km s⁻¹ (shown by the horizontal dashed line in

Figure 1(d)). MMS2 crossed the current sheet 260 ms after MMS1 and MMS3. During that time, the X-line moved an additional \sim 4 $d_{\rm e}$ in the +L-direction, as illustrated in Figure 1(o).

From the direction of the exhaust outflow jets $V_{\rm eL}$, we can deduce which side of the X-line the probes were located. MMS1 and MMS2 observed negative $V_{\rm eL}$ jets (Figure 1(d)), which means they were located on the left side of the X-line in the sketch shown in Figure 1(p). MMS3 and MMS4 were located on the right side of the X-line because the $V_{\rm eL}$ jets (at the current sheet midplane where $B_{\rm L}=0$) were directed in the +L-direction (more details are given in Section 3.3).

Using the configuration shown in Figure 1(o), and the X-line motion along L at +150 km s⁻¹, we can calculate the possible ranges of the distances from the X-line for each probe during the (45 ms) time the probes traversed the current sheet. We

begin with the placement of the X-line relative to the crossing by the first spacecraft (MMS4). Because MMS4 observed $+V_{\rm eL}$, the minimum distance between MMS4 and the X-line is zero. In the scenario that MMS4 is located at the X-line, the distances between the X-line and MMS1, MMS2, and MMS3 are 5 km (-L-direction), 5.25 km (-L-direction), and 2 km (+L-direction), respectively.

In the other possible scenario, because MMS1 observed $-V_{eL}$ and therefore had to be at a -L location, the maximum separation of MMS4 from the X-line in the +L-direction is when MMS1 is at the X-line. In this extreme case, MMS4 is 5 km (+L-direction) away from the X-line, MMS3 is 7 km (+Ldirection) away from the X-line because MMS1 and MMS3 crossed the current sheet at around the same time, and MMS2 is 0.25 km (-L-direction) away from the X-line. From these two extreme scenarios, the ranges of the X-line distance to the spacecraft are $[-5 d_e \text{ to } 0]$, $[-5.25 d_e \text{ to } -0.25 d_e]$, $[+2.0 d_e \text{ to }$ +7 $d_{\rm e}$], and [0 to +5 $d_{\rm e}$] for MMS1, MMS2, MMS3, and MMS4, respectively. Thus, the only free parameter in the estimation of the spacecraft locations in the reconnection configuration is where to place MMS4 relative to the X-line when that spacecraft crossed the current sheet. In Figure 1(0), we have chosen MMS4 to be $+1.5 d_{\rm e}$ distance away from the X-line placing MMS1, MMS3, and MMS2 (furthest) at -3.5 $d_{\rm e}$, +3.5 $d_{\rm e}$, and -3.75 $d_{\rm e}$ distances from the X-line, respectively. These result in spacecraft locations that are qualitatively consistent with the following:

- 1. Among the four spacecraft, MMS2 is likely furthest from the X-line, as indicated by the fastest outflow electron jet $\Delta V_{\rm eL}$, and the smallest values of $E_{||}$ and $j \cdot E'$ (to be described below).
- 2. MMS2 has the largest and widest exhaust jet $\Delta V_{\rm eL}$, which also suggests that it is the furthest away from the X-line.
- 3. MMS4 is closer to the X-line compared to MMS3 because $j \cdot E'$ is slightly larger at MMS4.

Thus, Figure 1(p) qualitatively represents the locations of the four MMS spacecraft along the *L*-direction in the X-line frame. In the following two sections, we describe the general observational signatures of electron-only reconnection, with particular emphasis on the inflow velocity signatures along *N*, and examine how the inflow signatures vary relative to the X-line.

3.3. Reconnection Layer Geometry and Additional Signatures

In this section we describe the plasma and field profiles from the four spacecraft, which reveal how the spatial profiles of the electron reconnection layer differ on opposite sides of the X-line, as well as how they depend on the distance from the X-line. Comparison with the PIC simulation (to be described in Section 4) will further demonstrate the dependencies. Importantly, it will provide further consistency checks of our proposed spacecraft locations relative to the X-line.

Figure 1(a) shows the crossings of the current sheet by the four MMS spacecraft, indicated by the transition of the reconnecting field component $B_{\rm L}$ from about $\sim +5$ nT to ~ -5 nT. The $B_{\rm L}$ reversal was first encountered by MMS4 (blue), followed MMS1 (black) and MMS3 (green) crossing the current sheet at around the same time, and MMS2 (red) at last.

In order to intercompare the spatial profiles observed by the four spacecraft, in Figures 1(b)–(m), we have shifted the times of the center of each current sheet crossing ($B_L = 0$) to line up with $B_L = 0$ at MMS3 (which is one of the two "middle" spacecraft) with MMS2 shifted by -25.05 ms, MMS1 shifted by +2.5 ms, and MMS4 shifted by +25.0 ms. The comparison yields the following notable features:

- 1. The peak of the out-of-plane magnetic field $B_{\rm M}$ (Figure 1(c)) is not centered at the current sheet midplane, and its location differs on the two sides on the X-line. On the left (-L side) of the X-line shown in Figure 1(p) (MMS1 and MMS2), the peak of $B_{\rm M}$ enhancement is shifted toward the leading edge of the current sheet (-N-direction), whereas on the +L side (MMS3 and MMS4), the peak of $B_{\rm M}$ enhancement is shifted toward the trailing edge side of the current sheet (in the +N-direction).
- 2. There was an external electron flow $V_{\rm eL}$ of $\sim +150$ km $\rm s^{-1}$ (marked by the horizontal dashed line) where all $V_{\rm eL}$ profiles converged at the two edges of the current sheet (Figure 1(d)). At the midplane ($B_L = 0$), MMS3 and 4 observed positive $\Delta V_{\rm eL}$ outflow jets (relative to the external flow), whereas MMS1 and 2 observed negative $\Delta V_{\rm eL}$ outflow jets. The negative jets (\sim -525 to -575 km $(\sim 175-225 \text{ km s}^{-1})$, with both jets being much faster than the upstream ion Alfvén speed of $\sim 25 \,\mathrm{km \ s^{-1}}$. Furthermore, MMS3 and 4 observed a reversed flow (toward the X-line) at the trailing edge of the current sheet, but MMS1 and 2 did not see toward-the-X-line flows at all. MMS2's jet was the widest and the largest, suggesting that the spacecraft was located farthest downstream from the X-line compared to the other spacecraft.
- 3. None of the spacecraft detected reconnection ion jets $V_{\rm iL}$ (Figure 1(e)). We note that MMS3's V_{iL} appears to have ion-jet-like signatures. However, this $V_{\rm iL}$ structure extends far beyond (to the right of) the current sheet. Additionally, MMS2's V_{iL} structure also appears to have ion-jet-like signatures, but it is directed opposite to MMS2's electron jets $V_{\rm eL}$ (Figure 1(d)), therefore not consistent with it being a reconnection ion outflow. The 20–30 km s⁻¹ ion flow enhancements are within the noise level of the 37.5 ms resolution FPI ion velocity moment data (see Figure 5 in Appendix). Furthermore, the ions are not coupled to the magnetic field in the electron-scale current sheet because the $(E \times B/B^2)_L$ velocity is at least 10 times larger than any $V_{\rm iL}$ enhancements, while the electrons are essentially coupled because their velocity $V_{\rm eL}$ follows $(E \times B/B^2)_{\rm L}$ (see Figure 6 in the Appendix).
- 4. The amplitudes of the out-of-plane current j_M (Figure 1(f)) for the four spacecraft were in the range of $2.9{\text -}3.2~\mu\text{A}~\text{m}^{-2}$, with the weakest current density at MMS2. MMS1 measured the narrowest j_M profile whereas MMS2, MMS3, and MMS4 measured similar widths in j_M . At the locations of peak j_M , the parallel electric fields E_{\parallel} (Figure 1(g)) also peaked (in amplitude) with values ranging from -3.5 to -7.51 mV m⁻¹, with the smallest amplitude at MMS2. Similarly, the nonideal magnetic-to-particle energy conversion measure $j \cdot E'$ (Figure 1(h)) also peaked approximately at the peak locations of j_M with values in the range $7.5{\text -}20.5$ nW m⁻³, and again weakest at MMS2. The measure

 $j \cdot E'$ is primarily dominated by $j_{\parallel} E_{\parallel}$ as seen in Figure 1(i). All these features suggest that MMS2 was furthest downstream of the X-line.

3.4. Observations of the Bipolar, Asymmetric, and Highly Variable Inflow Velocities

Perhaps the most dramatic difference observed at the four spacecraft is the electron inflow velocity $V_{\rm eN}$ (Figures 1(j)–(m)), despite the fact that the spacecraft separations were only a few electron inertial lengths ($d_{\rm e}$).

Figures 1(j)–(m) show that in the frame of the current sheet, which convects at a normal speed of -95 km s^{-1} , $V_{\rm eN}$ was bipolar, as expected of a reconnection inflow. However, the inflow velocity amplitudes among the spacecraft were very different, and two of the spacecraft (MMS2 and MMS3) observed highly asymmetric inflows.

On the left side of the X-line, MMS2 (Figure 1(j)), the spacecraft further away from the X-line, measured the largest asymmetry in the $V_{\rm eN}$ flows. MMS2 measured a peak positive $V_{\rm eN} \approx 365~{\rm km~s}^{-1}$ at the leading edge of the current sheet, and a peak negative $V_{\rm eN} \approx 100~{\rm km~s}^{-1}$ at the trailing edge, for a ratio of the two inflow speeds of ~ 3.65 .

Moving closer to the X-line on the left side, MMS1 (Figure 1(k)) measured much more symmetric inflow velocities, with a ratio of the two inflow velocities of ~ 1.7 .

On the right side of the X-line, MMS3 and MMS4 also measured bipolar electron inflows, however, the asymmetry flipped on this side. In other words, MMS3 and MMS4 measured $\Delta V_{\rm eN}$ smaller at the leading edge of the current sheet compared to the trailing edge (Figures 1(1) and (m)). MMS3 has a larger $V_{\rm eN}$ asymmetry (ratio of $\sim\!1.7$) and is also further away from the X-line compared to MMS4 (ratio of $\sim\!1.3$). Thus, there appears to be a pattern that the inflow asymmetry is larger further away from the X-line, and the sense of the asymmetry is opposite on the two sides of the X-line in the L-direction.

The average inflow speed (calculated from the peak inflow values on the two sides of the current sheet) was quite different at the different spacecraft: 233 km s $^{-1}$, 178 km s $^{-1}$, 204 km s $^{-1}$, and 134 km s $^{-1}$ at MMS2, MMS1, MMS4, and MMS3, respectively.

Interestingly, the average peak values of the inflows on the two sides of the current sheet normalized to the hybrid electron Alfvén speed given by $V_{\rm AeL} = [B_{\rm L1}B_{\rm L2}(B_{\rm L1} + B_{\rm L2})/(\mu_o\rho_1B_{\rm L2} + \mu_o\rho_2B_{\rm L1})]^{1/2}$, with subscripts 1 and 2 denoting the $|V_{\rm eN}|$ peak locations (the first and second pink dashed lines in Figures 1(j)–(m)) (Cassak & Shay 2007) revealed similar values among the spacecraft. From left to right, $V_{\rm AeL}$ is $\sim 1069~{\rm km~s^{-1}}, \sim 782~{\rm km~s^{-1}}, \sim 929~{\rm km~s^{-1}},$ and 813 km s⁻¹ at MMS2, MMS1, MMS4, and MMS3, respectively.

We define the relative inflow velocity as the difference between the peak values of $|V_{\rm eN}|$ on the two sides of the inflow region in the observations. In these normalized units, the average relative inflow velocity from left to right (in Figure 1(p)) were $\sim 0.22 \, V_{\rm AeL}, \, \sim \! 0.23 \, V_{\rm AeL}, \, \sim \! 0.22 \, V_{\rm AeL}, \,$ and $\sim \! 0.17 \, V_{\rm AeL}$ at MMS2, MMS1, MMS4, and MMS3, respectively.

In Section 4.2, we will explain how such an asymmetry in the inflow may arise with findings from the 2D electron-only simulation. Below we describe the simulation findings and perform a comparative analysis between the observations and 2D simulation.

3.5. General Features from the 2D Electron-only Reconnection Simulations

We performed 2D PIC simulations as described in Section 2.3 to investigate the inflow velocities generated in electron-only reconnection. We chose 2D instead of 3D to see whether the physics in a 2D system can already account for most of the key observational features, and it appears to be the case. Note that we use simulation parameters similar to the event in Figure 1, except with a guide field of 1 instead of 8. Increasing the guide field to 8 while maintaining the plasma beta introduces computational difficulties, because large temperatures together with larger guide fields (guide fields greater than 1) tend to produce significant PIC noise, thus making the determination of the reconnection electric field untenable. Additionally, a guide field of 1 is likely to produce qualitatively the same asymmetries in inflow velocities as with guide fields larger than 1.

The overall structure of the inflowing electrons is shown by $V_{\rm eN}$ (Figure 2(a)) in the reconnection plane. The image of $-\partial B_{\rm M}/\partial L$ in Figure 2(b) shows similar structure to $V_{\rm eN}$ (Figure 2(a)), indicating that the geometry of the magnetic field is related to the asymmetry in $V_{\rm eN}$ due to Ampere's law, which will be further discussed in Section 4.2. More quantitative comparisons between $V_{\rm eN}$ and $-\partial B_{\rm M}/\partial L$ are shown in Figures 3(i)–(1).

The electron jets $V_{\rm eL}$ (Figure 2(c)) are bounded within the separatrix line on both sides of the exhaust. The left (right) jets mostly lie above (below) the midplane of the current sheet. Significant toward-the-X-line flows are also present on one edge of each exhaust: at the bottom edge left of the X-line, and at the top edge to the right of the X-line.

The parallel electric field E_{\parallel} (Figure 2(d)) is localized within distances of a few $d_{\rm e}$ around the X-line. The out-of-plane magnetic field $B_{\rm M}$ (Figure 2(f)) shows a tilt in the reconnection plane, with enhanced $B_{\rm M}$ on the lower left and the upper right regions. The 1D cuts along N at different L locations in Figure 3(b) also show this feature.

A large out-of-plane current j_M (Figure 2(g)) is centered at the midplane with larger enhancements around the X-line. Lastly, the nonideal magnetic-to-particle energy conversion measure $j \cdot E'$ (Figure 2(h)) is most enhanced near the X-line.

4. Comparison of the Observed Plasma and Field Profiles with the Simulations

We now compare 1D cuts (Figure 3) from the 2D simulation along N at different L locations with the observations (Figure 1). Part of the comparison is to verify that the spacecraft positions deduced in Section 3.2 are qualitatively correct. The comparison also reveals interesting spatial structures of the electron reconnection layer that have never been studied before. For comparison, the cuts in Figure 3 are color coded similar to the MMS observations (Figure 1) based on their relative positions along L given in Figure 1(p). For example, the cut at L=19.12 is shown in red and represents the position of MMS2 and so on. In the simulation, for simplicity we opt to take cuts at equal intervals from the X-line whereas the cuts in the observations are most likely not equally spaced. Here we describe some similarities and differences between the observations and the simulation:

1. Similar to the observations (Figure 1(c)), the peak of the out-of-plane magnetic field $B_{\rm M}$ profile is not centered at

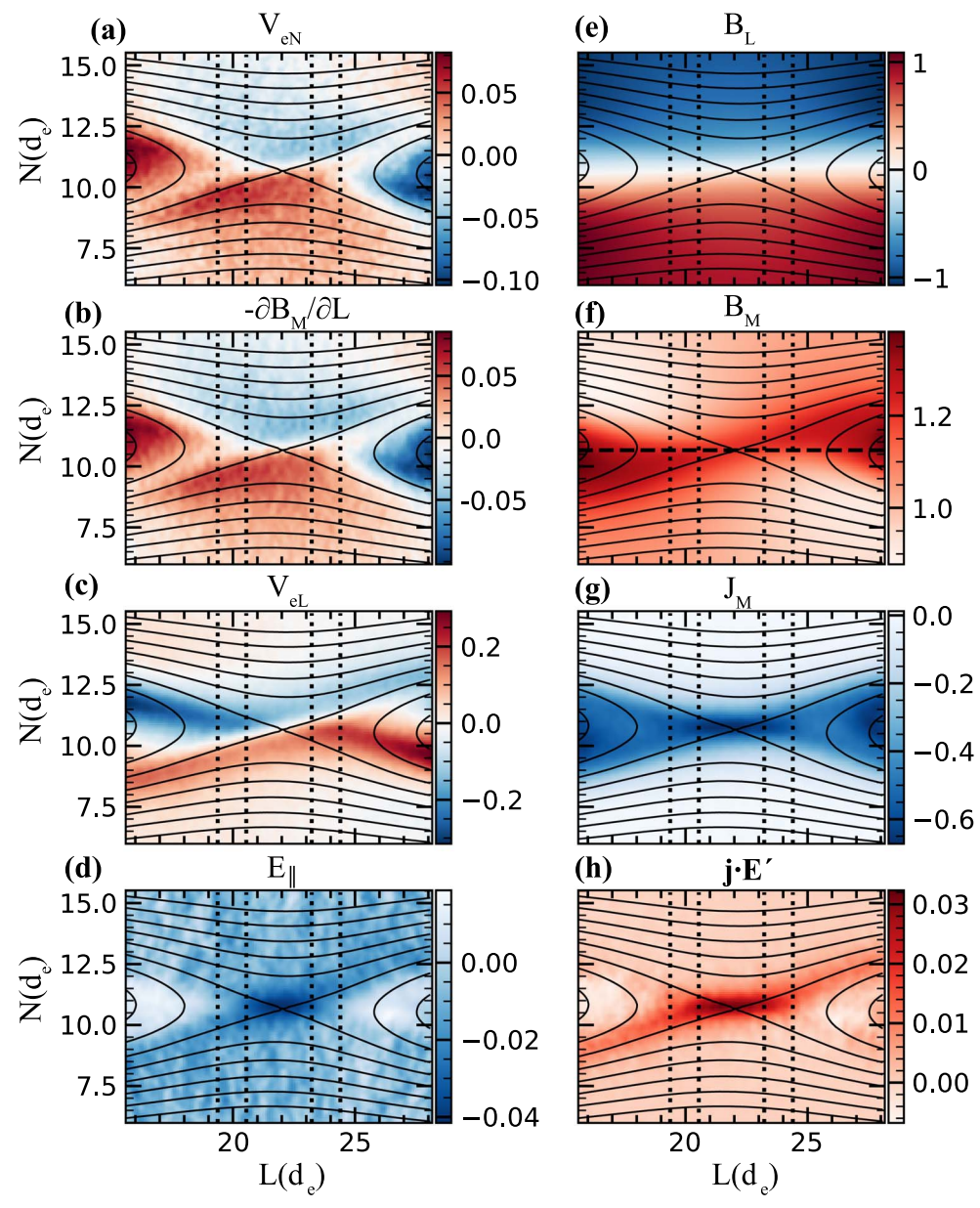


Figure 2. 2D morphology of electron-only reconnection shown in each panel: (a) converging inflows $V_{\rm eN}$ toward the midplane, (b) the gradient of the out-of-plane magnetic field $B_{\rm M}$ along L, (c) outflow jets $V_{\rm eL}$, (d) the parallel electric field E_{\parallel} , (e) the reconnection magnetic field $B_{\rm L}$, (f) tilted $B_{\rm M}$, (g) the out-of-plane current $j_{\rm M}$, and (h) the magnetic-to-particle energy conversion parameter $j \cdot E'$. The dotted vertical lines are the locations of the 1D cuts in Figure 3. The horizontal dashed line in (f) highlights the tilt of the guide field $B_{\rm M}$.

the current sheet midplane, and the shift is opposite on the two sides of the X-line. The red and black out-of-plane magnetic field $B_{\rm M}$ profiles (Figure 3(b)), presented as 1D cuts on the left side of the X-line, show a $B_{\rm M}$ peak shifted toward the leading edge of the current sheet, while the blue and green profiles, taken on the right side of the X-line, show a peak shifted toward the trailing edge.

- 2. There are slight differences in terms of the amplitude of the $B_{\rm M}$ peak. In the simulation, the downstream (red and green) profiles show larger $B_{\rm M}$ amplitudes than the (black and blue) profiles taken closer to the X-line. This feature is similar to the observed (red and black) profiles on the left side of the X-line (Figure 1(c)). Additionally, in the observations, the blue and green profiles of the guide field (Figure 1(c)) have almost equal $B_{\rm M}$ enhancements, which
- are not seen in simulation profiles (Figure 3(b)). One possible explanation for this discrepancy is that MMS3 and MMS4 were likely much closer to each other because their peak values and structures of $j_{\rm M}$ (Figure 1(f)) and $E_{||}$ (Figure 1(g)) were very similar, while the cuts in the simulation were taken at \sim 1.2 $d_{\rm e}$ apart. On the other hand, if the two spacecraft were very close, our assumption of a constant X-line drift in L would not be accurate. This is currently not understood and requires further investigation.
- 3. As pointed out in Section 3.5, the electron flows in the L-direction, $V_{\rm eL}$, show outflowing jets away from the X-line, as well as flows toward the X-line near one exhaust boundary on both sides of the X-line. This pattern is clearly seen in the 1D cuts as well (Figure 3(c)).

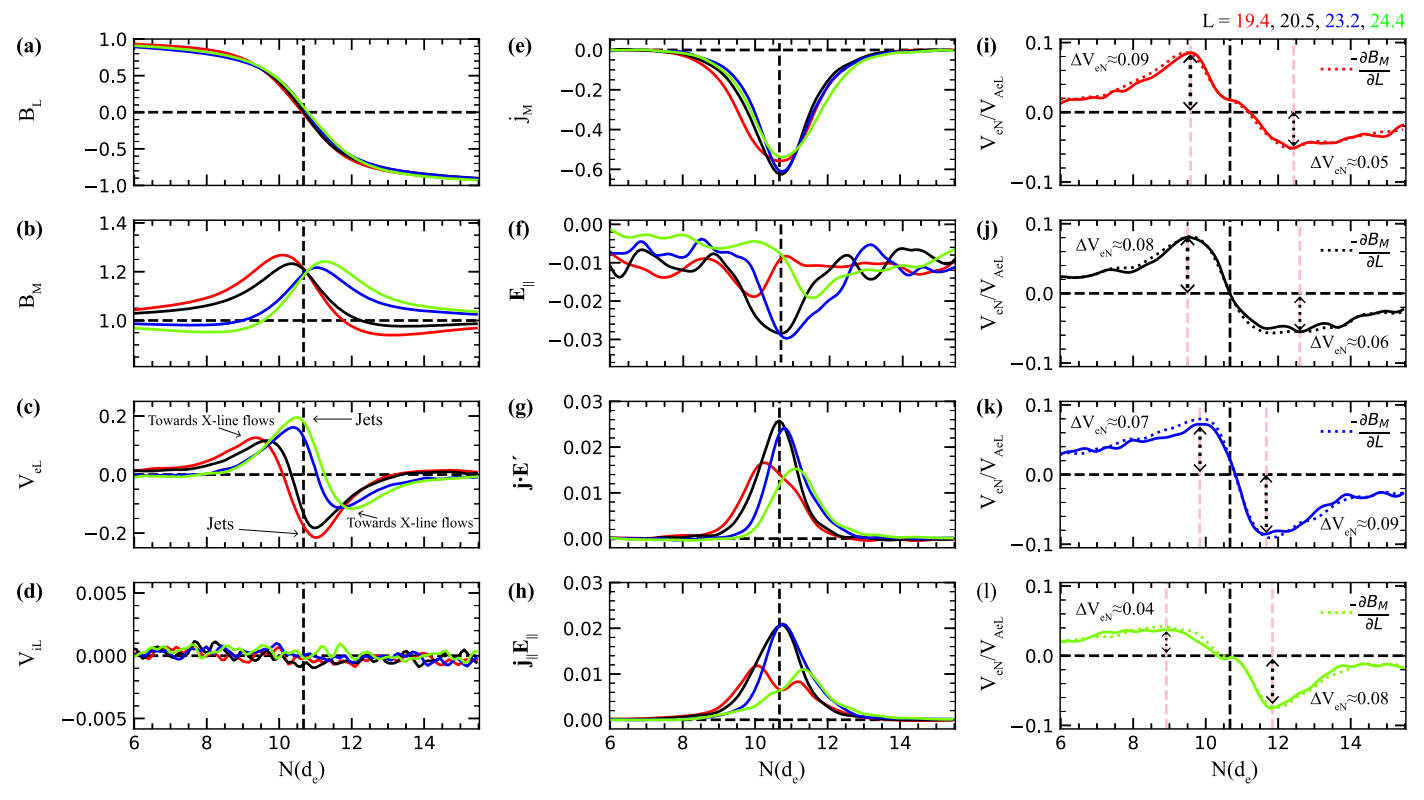


Figure 3. 1D simulation cuts of (a) the reconnecting magnetic fields $B_{\rm L}$, (b) the out-of-plane magnetic field $B_{\rm M}$, (c) the electron outflows $V_{\rm eL}$, (d) ion flows, (e) the out-of-plane current $j_{\rm M}$, (f) enhanced parallel electric field E_{\parallel} , (g) enhanced magnetic-to-particle energy conversion parameter $j \cdot E' \equiv j \cdot (E + V_e \times B)$, (h) $j_{\parallel} E_{\parallel}$, and (i–l) inflowing electrons $V_{\rm eN}$ (solid lines), shown at the locations of the dotted vertical lines in Figure 2. The inflows for all cuts are calculated in the normalized units of electron Alfvén speed given by $V_{\rm AeL} = [B_{\rm L1}B_{\rm L2}(B_{\rm L1} + B_{\rm L2})/(\rho_1B_{\rm L2} + \rho_2B_{\rm L1})]^{1/2}$, with subscripts 1 and 2 denoting the $|V_{\rm eN}|$ peak locations of the first and second pink dashed lines, respectively. The asymmetries in $V_{\rm eN}$ are larger for the cuts further away from the X-line and the asymmetry flips on the two sides of the outflow like observations in Figure 1. The electron inflows closely follow $-\partial B_{\rm M}/\partial L$ (dotted lines) for all the 1D cuts in the inflow region.

However, in the observations (Figure 1(d)), the toward-the-X-line electron flows were measured only on the right (+L) side of the X-line by MMS3 and MMS4.

- 4. The simulation showed negligible ion exhaust jets (Figure 3(d)), like the observations (Figure 1(e)), indicating electron-only reconnection.
- 5. In the simulation (Figure 3(e)), the out-of-plane current density $j_{\rm M}$ (Figure 3(e)) is slightly larger closer to the X-line, while the width is slightly larger further downstream. These trends are also present in the observations (Figure 1(f)), but not as clear. The small differences in $j_{\rm M}$ (and the associated $B_{\rm L}$) between the spacecraft indicate that $j_{\rm M}$ is not as localized as some other parameters.
- 6. The peak value of the parallel electric field E_{\parallel} (Figure 3(f)) is largest for the black and blue curves that are closest to the X-line but smallest for the red curve like MMS2 (Figure 1(g)). On the other hand, the peak values of E_{\parallel} in the observations (Figure 1(g)) on the right side (blue and green) are almost identical, perhaps due to their proximity, unlike the simulation where cuts are taken at equal length intervals.
- 7. The $j \cdot E'$ parameter (Figure 3(g)) is larger for cuts closer to the X-line and smaller for cuts away from the X-line, which is consistent with observations (Figure 1(h)). Finally, the main component contribution of $j \cdot E'$ comes from $j_{\parallel} E_{\parallel}$ as indicated in Figure 3(h), a feature that is also present in observations.

4.1. Comparison of the Observed and Simulated Electron Inflow Velocities

Cuts along the *N*-direction in Figures 3(i)–(l) taken on both sides of the X-line reveal the strong variation of $V_{\rm eN}$ with distance downstream of the X-line. On the far-left side, the positive and negative $V_{\rm eN}$ (Figure 3(i)) are highly asymmetric, similar to the MMS2 observation (Figure 1(j)). The cut closer to the X-line (black in Figure 3(j)) is much more symmetric, like MMS1 (Figure 1(k)). On the other side of the X-line, the two cuts of $V_{\rm eN}$ are also like MMS3 (Figure 1(m)) and MMS4 (Figure 1(l)), in that MMS4's inflow profile is more symmetric than MMS3's inflow profile.

The simulation also exhibits the reversal of inflow asymmetry on the opposite side of the X-line, similar to the MMS observations.

We again define the relative inflow velocity as the difference between the peak values of $|V_{\rm eN}|$ on the two sides of the inflow region in the simulation. The relative inflow velocities from left to right are $\sim 0.14\,V_{\rm AeL}$, $\sim 0.14\,V_{\rm AeL}$, $\sim 0.15\,V_{\rm AeL}$, and $\sim 0.12\,V_{\rm AeL}$, respectively. The red cut (Figure 3(i)) measured a relative inflow velocity similar to the cuts closer to the X-line, consistent with the observations when normalized to the electron Alfvén speed $V_{\rm AeL}$. The two cuts closer to the X-line (black and blue) in Figures 3(j) and (k) have similar relative inflow velocities, which are also present in the observations (black and blue) in Figures 1(k) and (l), respectively. Lastly, the far-right cut (green) in Figure 3(l) measured the smallest

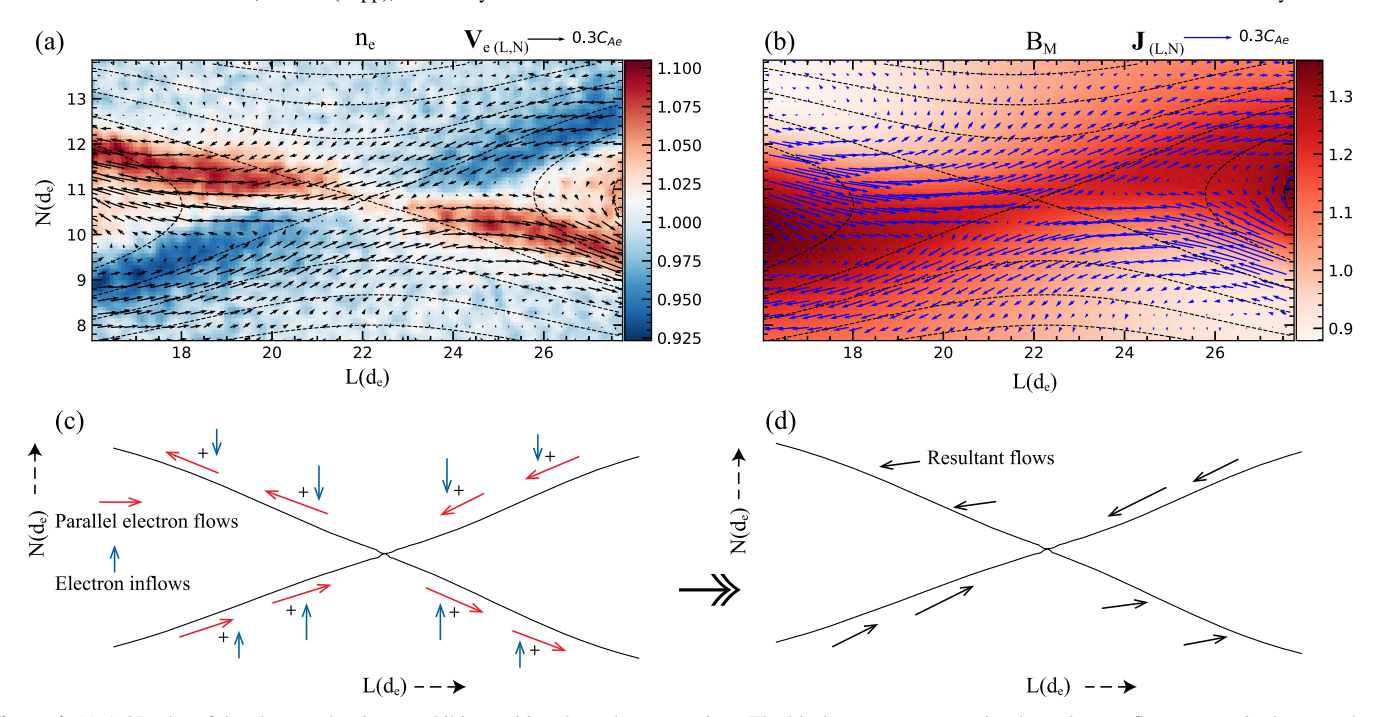


Figure 4. (a) A 2D plot of the electron density $n_{\rm e}$ exhibits cavities along the separatrices. The black arrows represent in-plane electron flows $V_{\rm e(L,N)}$ in the L-N plane. The electrons are flowing toward the X-line where the density depletes due to the parallel electric field. (b) A 2D plot of the out-of-plane magnetic field is overlaid with in-plane currents $j_{(L,N)}$ showing enhancement where the currents rotates. The magnitude of the electron flows and the currents in (a) and (b) are shown at the top right of their respective panels. (c) Schematics of the parallel flows and the reconnection-mediated inflows in the inflow region are shown by blue (electron inflows) and red (electron parallel flows) arrows. (d) The resultant vectors from the addition of the parallel flows and the reconnection-mediated inflows in (c) are shown by the black arrows. The black arrows in the inflow region is similar to the vector arrows in (a) along the separatrices.

relative inflow velocity, which is consistent with the observations (Figure 1(m)).

In the simulation, the asymmetry of the inflow between the top and bottom region is about a factor of two, while in the observations the asymmetry factor can be as large as four times. The difference could be due to the fact that our simulation uses a guide field of unity whereas the MMS-observed guide field was eight. Since the guide field appears to be the cause of the inflow asymmetry, one would therefore expect the asymmetry to be larger in the observations than in the simulations. What is currently not understood is why MMS2 observed by far the largest amplitude of $V_{\rm eN}$, while the simulation does not produce such a drastic variation between the different cuts. We note that the substantially larger $B_{\rm M}$ at MMS2 may be related to this as well. This may point to temporal or 3D effects for MMS2.

4.2. Origin of the Inflow Asymmetry

The tilting of the reconnection plane even in standard ion-coupled reconnection without an initial guide field has been studied in the presence of tangential shear flows (Cassak 2011). Observations and simulation findings of guide field reconnection have also reported asymmetry of the Hall fields even in moderate guide field cases (Eastwood et al. 2010). Large guide field observations (Øieroset et al. 2016) also revealed a significantly skewed Hall magnetic field with density perturbations. Thus, it is likely that such reconnection systems will also exhibit asymmetry in $V_{\rm eN}$ in the vicinity of the X-line. Previous numerical studies of guide field reconnection also reported an asymmetry in $V_{\rm eN}$ (Pritchett & Coroniti 2004), where the parallel electric field is enhanced along low-density separatrices. This parallel electric field produces parallel motion of

electrons along the separatrices (Drake et al. 2005), which dictates the structure of the guide field.

The initial flows in our simulation are parallel to the magnetic field by virtue of the force-free configuration. After the reconnection onset, the parallel electric field produced along the bottom-left and top-right separatrices (Figures 2(d) and 3(f)) accelerates electrons toward the X-line forming the depletion of density, as shown in Figure 4(a). The black arrows in Figure 4(a) are electron flows $V_{\rm e(L,N)}$ in the reconnection plane. Moving in the opposite direction of the electron flows are the in-plane currents $j_{\rm (L,N)}$ shown in Figure 4(b) with the blue arrows. As seen in Figure 4(b), the guide field structure is enhanced where the change in the direction of the current is the largest. For instance, the bottom-left and top-right quadrants are where the current rotates collocatingly with the enhanced regions of $B_{\rm M}$.

The electron flows in Figure 4(a) are combinations of the parallel flows along the magnetic separatrices and the reconnection driven inflows as shown in the schematics in Figures 4(c) and (d). The parallel separatrix flows in Figure 4(c) are shown by the red arrows whereas the inflows due to reconnection are shown by the blue arrows. The addition of the N component of the parallel flows and the usual reconnection inflows produces enhanced inflows along the bottom-left and the top-right separatrices while reducing the inflow strengths along the two other separatrices. The combined effect of the parallel separatrix flows and the reconnection inflows, as shown in Figure 4(d), produces the asymmetry in the inflowing electrons.

The in-plane electron velocity $V_{\mathrm{e(L,N)}}$ and associated current are linked to the structure of the guide field through the relation $V_{\mathrm{e(L,N)}} = -c/(4\pi ne) \boldsymbol{\nabla} B_{\mathrm{M}} \times \boldsymbol{M}$ (from Ampere's law ,with \boldsymbol{M} the unit vector along the M-direction) with uniform unit density

and no ion currents. This relation is exact for a 2D system. Note that, in our normalized units, $V_{\rm e(L,N)} = -\sqrt{(m_e/m_i)}\, \nabla B_{\rm M} \times M$ or $V_{\rm eN} = -\sqrt{(m_e/m_i)}\, \partial B_{\rm M}/\partial L$. The good agreement between $-\partial B_{\rm M}/\partial L$ and $V_{\rm eN}$ is evident in Figures 2(a) and (b) $(-\partial B_{\rm M}/\partial L$ is multiplied by a factor of $\sqrt{(m_e/m_i)}$ in Figures 2(b) and 3(i)–(l)). When the guide field has a tilt, as shown in Figure 2(f), and $-\partial B_{\rm M}/\partial L$ is nonzero, there is an associated asymmetry in $V_{\rm eN}$. 1D cuts of $-\partial B_{\rm M}/\partial L$ along N at different outflow locations are shown in Figures 3(i)–(l) and match very well with corresponding cuts of $V_{\rm eN}$.

Initially, the out-of-plane magnetic field $B_{\rm m}$ is uniform along L. The parallel current perturbs $B_{\rm m}$, but it is only after the reconnection onset when the guide field structure starts to tilt significantly. The tilt of the guide is consistently generated to follow the asymmetry of the inflows as demonstrated by the Ampere's relation above. Within a distance of 5 $d_{\rm e}$ from the X-line, this asymmetry becomes pronounced downstream of the X-line where the separatrix flows are large.

5. Summary and Discussion

We have presented significant spatial variability of electron inflows within a few $d_{\rm e}$ distances from the X-line in the electron-only reconnection event observed by the MMS spacecraft in the Earth's turbulent magnetosheath downstream of the quasi-parallel bow shock region. All four spacecraft distances from the X-line were less than 7 $d_{\rm e}$. We summarize the main findings here.

- 1. The MMS spacecraft observed the presence of large asymmetries in the electron inflows, with the inflow on the two sides of the reconnecting current layer differing as much as a factor of \sim 4. Even though the spacecraft were only separated by 7 $d_{\rm e}$, the degree of inflow asymmetry was significantly different at the different spacecraft. Specifically, the inflow asymmetry increased with distance from the X-line and the asymmetry was opposite on opposite sides of the X-line (along the L-direction).
- 2. The average normalized electron inflows were \sim 0.21 $V_{\rm AeL}$, \sim 0.23 $V_{\rm AeL}$, \sim 0.22 $V_{\rm AeL}$, and \sim 0.17 $V_{\rm AeL}$ at MMS2, MMS1, MMS4, and MMS3, respectively, with an average value of \sim 0.21 $V_{\rm AeL}$. The electron inflows can be linked to the reconnection rate. However, our findings indicate that this may not be straightforward in the presence of a strong guide field compared with the case of a weak guide field. In the upstream region, the inflow velocity is given by the $E \times B$ drift, $v_{eN} \approx v_{e\perp,N} = \frac{(E \times B)_N}{B^2} = \frac{E_L B_M}{B^2} \frac{E_M B_L}{B^2}$, where $v_{e\perp}$ is perpendicular to the magnetic field. For a weak guide field, the term proportional to E_M in the equation for V_{eN} dominates and the reconnection rate directly follows from V_{eN} . However, for a strong guide field both the observations and the simulation reveal that $\frac{E_L B_M}{B^2}$ produces the dominant contribution to V_{eN} . Therefore, calculating the reconnection rate E_M in cases with a strong guide field is a greater challenge.

- 3. Comparison of the MMS observations with the 2D kinetic PIC simulation yielded similar field and plasma profiles, with the observed asymmetries being consistent with the presence of a guide field. For example, the peak of $B_{\rm M}$ enhancement shifted below the midplane on the left side of the X-line and above the midplane on the right side of the X-line for both the simulation and observations. Like the observations, the simulation also produced the toward-the-X-line flows on one side of the X-line, largest out-of-plane current $j_{\rm M}$, and parallel electric field $E_{||}$ closer to the X-line. These agreements between the observations and the simulation further confirm that the event was indeed electron-only reconnection.
- 4. The 2D simulation reproduced the same asymmetry pattern in the inflows $V_{\rm eN}$ observed by the MMS spacecraft. The parallel separatrix flows combine with the reconnection-mediated inflows and produce enhanced inflows along the bottom-left and the top-right separatrices while reducing inflow strengths along the other two separatrices. The sum of these two flows produces the asymmetry in the inflowing electrons in the simulation and spacecraft data.
- 5. The 2D simulation was not able to reproduce electron inflows as large as the values around $\sim 0.2~V_{\rm AeL}$ measured in the observations. The electron inflows in the 2D simulation are approximately half of those in the observations, i.e., about $\sim 0.1~V_{\rm AeL}$. In a previous simulation study of electron-only reconnection the strength of the electron inflows increased by a factor of two in 3D in comparison to 2D for the same plasma parameters used in the current 2D simulation (Pyakurel et al. 2021). Thus, 3D electron reconnection in simulations might yield inflow velocities closer to those measured in observations.

This research was supported by NSF grants No. AGS-2024198, No. PHY2109083 and NASA grants Nos. 80NSSC21K1481, 80NSSC20K1781, 80NSSC22K0352, 80NSSC20K1813 and NASA contract NNG04EB99C (at SWRI). We acknowledge high-performance computing support from Cheyenne provided by NCAR's CISL, sponsored by the NSF. This research also used NERSC resources; a U.S. DOE office of Science User Facility operated under Contract No. DE-AC02-05CH11231.

Appendix Absence of Reconnection Ion Jetting and Ion Coupling to the Magnetic Field in the Current Sheet

In this appendix, we report two figures. In Figure 5, a large-scale context of the thin current sheet illustrating the fact that the electron-scale current sheet was not embedded inside an ion-scale current is shown for MMS3. In Figure 6, the $(E \times B/B^2)_{L,N}$ velocities along with the ion and electron flows in the L- and N-directions are plotted, showing that the ions at MMS3 are not coupled to the magnetic field.

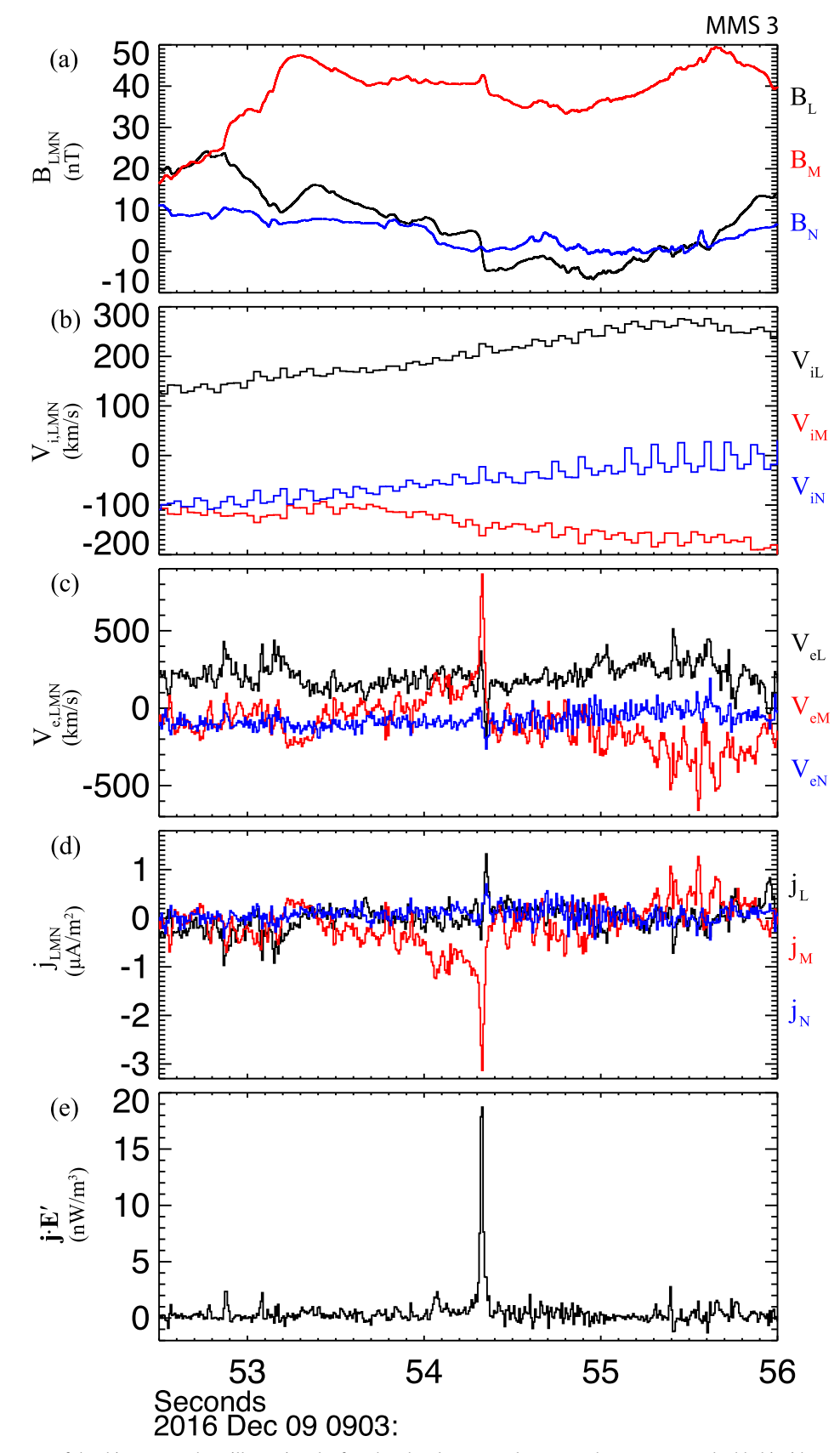


Figure 5. Large-scale context of the thin current sheet illustrating the fact that the electron-scale current sheet was not embedded inside an ion-scale current is shown for MMS3. Data are shown in the LMN coordinates determined for the thin current sheet and used in Figure 1. (a) Magnetic field. (b) Ion velocity. (c) Electron velocity. (d) Current density. (e) $j \cdot (E + V_e \times B) = j \cdot E'$. The thin reconnecting current sheet stands out in this interval, with nothing else approaching its current density or its value of $j \cdot (E + V_e \times B)$. The absence of an ion-scale current sheet enveloping the electron-scale current sheet is indicated by the fact that $|B_L|$ reaches essentially its asymptotic values immediately outside the thin current sheet.

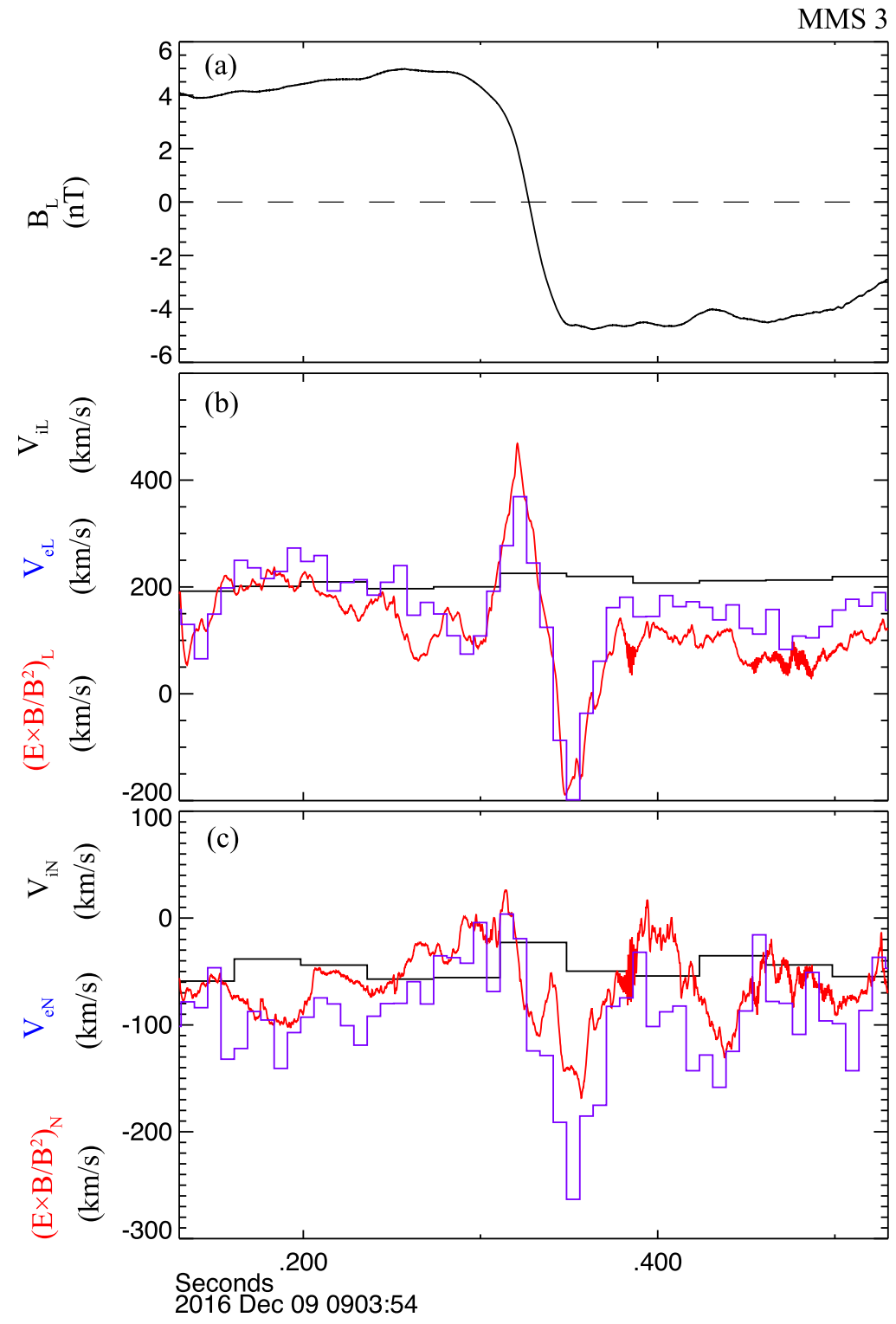


Figure 6. MMS3 data illustrating no ion coupling with the magnetic field. The reconnection magnetic field B_L (a) and the ion, electron, and $E \times B/B^2$ flow speeds in the L- (b) and N-directions (c) are shown in the same time interval as in Figure 1.

ORCID iDs

P. S. Pyakurel https://orcid.org/0000-0003-4832-7638

T. D. Phan https://orcid.org/0000-0002-6924-9408
J. F. Drake https://orcid.org/0000-0002-9150-1841
M. A. Shay https://orcid.org/0000-0003-1861-4767
C. C. Haggerty https://orcid.org/0000-0002-2160-7288
J. L. Burch https://orcid.org/0000-0003-0452-8403
D. J. Gershman https://orcid.org/0000-0003-1304-4769
R. B. Torbert https://orcid.org/0000-0001-7188-8690
R. J. Strangeway https://orcid.org/0000-0001-9839-1828
C. T. Russell https://orcid.org/0000-0003-1639-8298

References

```
Burch, J. L., Torbert, R. B., Phan, T. D., et al. 2016, Sci, 352, aaf2939
Burch, J. L., Webster, J. M., Hesse, M., et al. 2020, GeoRL, 47, e2020GL089082
Cassak, P. A. 2011, PhPl, 18, 072106
Cassak, P. A., & Shay, M. A. 2007, PhPl, 14, 102114
Drake, J. F., Shay, M. A., Thongthai, W., & Swisdak, M. 2005, PhRvL, 94, 095001
Eastwood, J. P., Shay, M. A., Phan, T. D., & Øieroset, M. 2010, PhRvL, 104, 205001
```

```
Eriksson, S., Wilder, F. D., Ergun, R. E., et al. 2016, PhRvL, 117, 015001
Gingell, I., Schwartz, S. J., Eastwood, J. P., et al. 2019, GeoRL, 46, 1177
Gosling, J. T., & Phan, T. D. 2013, ApJL, 763, L39
He, J.-S., Marsch, E., Tu, C.-Y., et al. 2011, JGRA, 116, A06207
Lavraud, B., Zhang, Y. C., Vernisse, Y., et al. 2016, GeoRL, 43, 3042
Mandt, M. E., Denton, R. E., & Drake, J. F. 1994, GeoRL, 21, 73
Øieroset, M., Phan, T. D., Haggerty, C., et al. 2016, GeoRL, 43, 5536
Phan, T. D., Eastwood, J. P., Cassak, P. A., et al. 2016, GeoRL, 43,
Phan, T. D., Eastwood, J. P., Shay, M. A., et al. 2018, Natur, 557, 202
Pritchett, P. L., & Coroniti, F. V. 2004, JGRA, 109, 1220
Pyakurel, P., Shay, M. A., Phan, T. D., et al. 2019, PhPl, 26, 082307
Pyakurel, P. S., Shay, M. A., Drake, J. F., et al. 2021, PhRvL, 127, 155101
Rager, A. C., Dorelli, J. C., Gershman, D. J., et al. 2018, GRL, 45, 578
Russell, C. T., Anderson, B. J., Baumjohann, W., et al. 2016, SSRv, 199,
Shay, M. A., Drake, J. F., Denton, R. E., & Biskamp, D. 1998, JGR, 103, 9165
Sonnerup, B. U. Ö. 1979, in Solar System Plasma Physics, Vol. 3 ed.
  L. J. Lanzerotti, C. F. Kennel, & E. N. Parker (Amsterdam: North-Halland)
Stawarz, J., Eastwood, J., Phan, T., et al. 2019, ApJL, 877, L37
Stawarz, J. E., Eastwood, J. P., Phan, T. D., et al. 2022, PhPl, 29, 012302
Torbert, R. B., Russell, C. T., Magnes, W., et al. 2016, SSRv, 199, 105
Vasyliunas, V. M. 1975, RvGeo, 13, 303
Wang, S., Chen, L.-J., Bessho, N., et al. 2019, GeoRL, 46, 562
Wilder, F. D., Ergun, R. E., Eriksson, S., et al. 2017, PhRvL, 118, 265101
Zeiler, A., Biskamp, D., Drake, J. F., et al. 2002, JGRA, 107, 1230
```